

University of Wollongong

Research Online

Faculty of Engineering and Information
Sciences - Papers: Part B

Faculty of Engineering and Information
Sciences

2020

Dehydration-Triggered Ionic Channel Engineering in Potassium Niobate for Li/K-Ion Storage

Shilin Zhang

University of Wollongong, sz384@uowmail.edu.au

Qining Fan

University of Wollongong, qf553@uowmail.edu.au

Yelin Liu

University of Wollongong, yl908@uowmail.edu.au

Shibo Xi

Xiufang Liu

xl222@uow.edu.au

See next page for additional authors

Follow this and additional works at: <https://ro.uow.edu.au/eispapers1>



Part of the [Engineering Commons](#), and the [Science and Technology Studies Commons](#)

Recommended Citation

Zhang, Shilin; Fan, Qining; Liu, Yelin; Xi, Shibo; Liu, Xiufang; Wu, Zhibin; Hao, Junnan; Pang, Wei Kong; Zhou, Tengfei; and Guo, Zaiping, "Dehydration-Triggered Ionic Channel Engineering in Potassium Niobate for Li/K-Ion Storage" (2020). *Faculty of Engineering and Information Sciences - Papers: Part B*. 4006.
<https://ro.uow.edu.au/eispapers1/4006>

Research Online is the open access institutional repository for the University of Wollongong. For further information contact the UOW Library: research-pubs@uow.edu.au

Dehydration-Triggered Ionic Channel Engineering in Potassium Niobate for Li/K-Ion Storage

Abstract

© 2020 WILEY-VCH Verlag GmbH & Co. KGaA, Weinheim Boosting charge transfer in materials is critical for applications involving charge carriers. Engineering ionic channels in electrode materials can create a skeleton to manipulate their ion and electron behaviors with favorable parameters to promote their capacity and stability. Here, tailoring of the atomic structure in layered potassium niobate (K₄Nb₆O₁₇) nanosheets and facilitating their application in lithium and potassium storage by dehydration-triggered lattice rearrangement is reported. The spectroscopy results reveal that the interatomic distances of the Nb–O coordination in the engineered K₄Nb₆O₁₇ are slightly elongated with increased degrees of disorder. Specifically, the engineered K₄Nb₆O₁₇ shows enhanced electrical and ionic conductivity, which can be attributed to the enlarged interlamellar spacing and subtle distortions in the fine atomic arrangements. Moreover, subsequent experimental results and calculations demonstrate that the energy barrier for Li⁺/K⁺ diffusion is significantly lower than that in pristine K₄Nb₆O₁₇. Interestingly, the diffusion coefficient of K⁺ is one order of magnitude higher than that of Li⁺, and the engineered K₄Nb₆O₁₇ presents superior electrochemical performance for K⁺ to Li⁺. This work offers an ionic engineering strategy to enable fast and durable charge transfer in materials, holding great promise for providing guidance for the material design of related energy storage systems.

Disciplines

Engineering | Science and Technology Studies

Publication Details

Zhang, S., Fan, Q., Liu, Y., Xi, S., Liu, X., Wu, Z., Hao, J., Pang, W., Zhou, T. & Guo, Z. (2020). Dehydration-Triggered Ionic Channel Engineering in Potassium Niobate for Li/K-Ion Storage. *Advanced Materials*,

Authors

Shilin Zhang, Qining Fan, Yelin Liu, Shibo Xi, Xiufang Liu, Zhibin Wu, Junnan Hao, Wei Kong Pang, Tengfei Zhou, and Zaiping Guo

Dehydration-triggered Ionic Channel Engineering in Potassium Niobate for Li / K ion Storage

Shilin Zhang^a, Qining Fan^a, Ye Liu^a, Shibo Xi^b, Xiufan Liu^c, Zhibin Wu^a, Junnan Hao^a, Wei Kong Pang^a, Tengfei Zhou^{a}, Zaiping Guo^{a*}*

[a] Institute for Superconducting and Electronic Materials, School of Mechanical, Materials, Mechatronics and Biomedical Engineering, University of Wollongong, Wollongong, 2522, Australia

[b] Institute of Chemical and Engineering Sciences A*STAR, Singapore, Singapore

[c] Key Laboratory of Pesticide & Chemical Biology of the Ministry of Education, Institute of Environmental & Applied Chemistry, Central China Normal University, Wuhan, 430079, PR China.

*Corresponding authors: Email: tengfeiz@uow.edu.au (T.F.Z); zguo@uow.edu.au (Z.P.G)

1 **Abstract:** Boosting the charge transfer in materials is critical for applications involving charge carriers.
2 Engineering the ionic channels in electrode materials can create a skeleton to manipulate their ion and
3 electron behaviors with favorable parameters to promote the capacity and stability of electrodes. Here,
4 we report tailoring of the atomic structure in layered potassium niobate ($\text{K}_4\text{Nb}_6\text{O}_{17}$) nanosheets and
5 facilitating their application in lithium and potassium storage by dehydration-triggered lattice
6 rearrangement. The X-ray absorption fine structure spectroscopy and electron paramagnetic resonance
7 results reveal that the interatomic distances of the Nb-O coordination in the engineered $\text{K}_4\text{Nb}_6\text{O}_{17}$
8 nanosheets are slightly elongated and their degrees of disorder is considerably increased. Specifically,
9 the engineered $\text{K}_4\text{Nb}_6\text{O}_{17}$ shows enhanced electrical and ionic conductivity, which could be attributed
10 to the enlarged interlamellar spacing and subtle distortions in the fine atomic arrangements. Moreover,
11 subsequent experimental results and density functional theory calculations demonstrate that the energy
12 barrier for Li^+/K^+ diffusion is significantly lower than that in pristine $\text{K}_4\text{Nb}_6\text{O}_{17}$. Interestingly, the
13 diffusion coefficient of K^+ is one order of magnitude higher than that of Li^+ , and the engineered
14 $\text{K}_4\text{Nb}_6\text{O}_{17}$ presents superior specific and rate capability for K^+ ions to Li^+ ions. This work offers an
15 ionic engineering strategy to enable fast and durable charge transfer in materials, holding great promise
16 for developing batteries as well as providing guidance for the material design of related energy storage
17 and conversion systems.

1. Introduction

Engineering structures at the atomic level, including grain boundaries, edges, and point defects, has aroused renewed interest recently as the pivotal strategy for directing their physicochemical behaviors,^[1-3] in several ways that are particularly desirable for electrochemical ions storage relying on reversible ionic (de)intercalation of metal ions, such as Li^+ ,^[4] Na^+ ,^[5] Mg^{2+} ,^[6] Zn^{2+} ,^[7] etc. In the ionic batteries, this involves the shuttling and storage of ions between two electrodes, coupled with the flow of electrons in an external circuit. Therefore, efficiently delivering sufficient numbers of ions through ionic channels in the electrode is the main factor needed to achieve elevated energy density under a high current rate.^[8] To address the charge transport limitations of electrodes, constructing interconnected ionic channels can offer highly efficient charge delivery.^[9] Meanwhile, the introduction of tailoring materials at the atomic level is more effective and does not require sacrificing the energy density of the electrode.^[10, 11] Recently, studies have reported the inner channel for ionic transport in materials and the external ionic diffusion from the electrolyte to the channels are two main factors influencing the ionic kinetics.^[12] Regulating the channels in the electrodes will promote the mobility and diffusion kinetics of exotic ions.^[13] For example, graphite, the commercialized anode for lithium ion batteries (LIBs), has shown an inferior capacity when being utilized for sodium ion batteries due to the insufficient interlayer spacing and unaffordable energy barrier for intercalation/extraction of Na^+ ions.^[14] In contrast, expanded graphite with a wider atomic interlayer spacing shows improved capability for Na^+ storage.^[15]

A “blended cocktail strategy” with precise control and construction of high electronic conductivity and interconnected ionic channels may hold the key to optimizing the energy performance of batteries. Currently, most of the primary investigation of other types of metal ion batteries have investigated replacements from previously successful electrodes in LIBs, including carbonaceous materials,^[16, 17] alloy based compounds,^[18] and sulfides.^[19]

1 Interestingly, a recent work reported that niobium based electrode materials possessing
2 fascinating properties, such as an intercalation-type mechanism, rich redox chemistry, and
3 achievable scalability at a practical level, have been identified as ideal candidates for
4 rechargeable metal ion batteries.^[20] Moreover, a higher working voltage (above 1.0 V vs Li⁺/Li)
5 compared to graphite can restrain electrolyte decomposition and dendrites formation, ensuring
6 the safety of batteries.^[21] Octahedral subunits in the crystal structure linked through edge-
7 and/or corner-sharing type arrangements guarantee excellent structural stability.^[22]
8 Nevertheless, the fine structure of niobium based anodes for LIBs needs to be readjusted when
9 they are applied in other battery technologies, due to the changes in diffusion properties or
10 interfacial compatibility. Engineering niobium based anodes that possess excellent electronic
11 and superior ionic conductivities is a highly attractive strategy, which can be possibly achieved
12 by lattice rearrangement at the atomic level.

13 To this end, by taking layered potassium niobate (K₄Nb₆O₁₇, KNO) as a model, recruiting
14 crystal water to force the ionic channels to undergo a lattice structure transition, is first
15 presented and designed for both Li and K ion storage. The constructed hierarchical ionic
16 pathways are beneficial to synergistically endow the electrodes with quick ion transfer by virtue
17 of expanded lattice spacing and in-plane/interlamination channels. A reduced transfer kinetics
18 barrier, increased ion diffusion paths, and reduced energy gap in the engineered KNO could be
19 achieved via fine atomic rearrangement. As a consequence, the engineered KNO can provide
20 ionic diffusion coefficients that are an order of magnitude higher, three times higher capacity
21 output, and extended cycle life compared to pristine KNO. Our work opens a new avenue for
22 the design of electrode materials with excellent charge transfer parameters via dehydration for
23 energy storage and conversion applications.

24 2. Results and discussion

The engineered KNO can be facilely achieved through intercalation of water molecules followed by a dehydration process at a modest temperature. In this route, the interlayer spacing could be initially expanded by crystal water acting as pillars. After thermal treatment under mild conditions, hierarchical ionic channels can be thus built up with defects and in-plane/interlamination diffusion pathways (**Scheme 1**).

As displayed in **Figure 1a**, all diffraction peaks of the samples match well with those of the standard orthorhombic $\text{K}_4\text{Nb}_6\text{O}_{17}$ (JCPDS No. 04-010-2507).^[23] The observed d_{040} value of 10.9 Å can be assigned to $\text{K}_4\text{Nb}_6\text{O}_{17} \cdot 4.5\text{H}_2\text{O}$ after the intercalation of water molecules.^[24] The basal (*010*) reflection peaks are observed to shift to lower angles after the water intercalation compared with those of standard KNO samples (blue dots in **Figure 1a**). After the dehydration at 350 °C (details in the Synthesis methods), the peak of the KNO/rGO still located at lower degree compared to the standard orthorhombic $\text{K}_4\text{Nb}_6\text{O}_{17}$ with reduced intensity, suggesting that the decreased crystallinity of KNO is due to the elimination of intercalated water molecules.^[25] Notably, the d_{040} value of KNO/rGO is 9.0 Å, which is 0.6 Å larger than that of the standard orthorhombic $\text{K}_4\text{Nb}_6\text{O}_{17}$ (8.4 Å) (**Figure 1a** and **Figures S1 to S3** in the Supporting Information), signifying the enlarged lattice spacing compared to that of standard KNO. These expanded interlayer spaced in KNO/rGO could serve as ionic channels to enable the insertion of larger cations into the crystal structure. Meanwhile, the structural difference can be further understood from Raman spectroscopy (**Figure 1b**). Three dominant peaks are present at around 230, 650, and 900 cm^{-1} , corresponding to the Nb-O-Nb bending, slightly distorted Nb-O bond stretching of edge-sharing NbO_6 octahedra, and terminal highly distorted Nb=O bond stretching, respectively. In addition, with a higher degree of Nb-O bond order, the bond lengths will be shortened, and the Raman peaks will shift to higher wavenumbers.^[26] In this work, for pristine KNO, a sharp peak can be found at around 900 cm^{-1} , while the intensity of this peak is significantly reduced in both KNO-200 (dehydration at 200 degree) and

KNO/rGO. The intensity ratio (I_{650}/I_{900}) between the two peaks at 650 and 900 cm^{-1} changes from 0.33 (pristine KNO) to 1.13 (KNO-200) and then to 10.0 (KNO/rGO). The intensity ratio, which increasingly changes from 0.33 to 10.0 clarifies the dominant contribution of the slightly distorted bonds at around 650 cm^{-1} , which further indicates that more structural flexibility could be achieved in KNO/rGO.^[25] This phenomenon is well consistent with our XRD results (Figure S2a), that is, lower crystallinity, increased interlayer/atomic distances, and higher structural flexibility can be achieved via the dehydration process. This flexible host will possibly be beneficial to the fast mobility and diffusion kinetics of exotic ions.

The scanning electron microscopy (SEM) and transmission electron microscopy (TEM) images in **Figures 1c, 1d, and S4**, verify the morphology of abundant nanosheets with sizes up to several micrometers in KNO/rGO. The lateral size of the constituent nanosheets is in the range of 100–200 nm (**Figure S4b**). Moreover, the high-resolution TEM (HRTEM) images (**Figure 1e, and S4d**) demonstrate that the layered structure of KNO/rGO with its porous distribution can be well preserved after thermal treatment. The interatomic distances of a selected area were determined to be 8.9 and 3.3 Å, standing for the (040) facet and (002) reflection of the lamellar KNO structure, respectively (**Figure 1e**). This result is also supported by the selected area electron diffraction (SAED) pattern (**Figure 1f**). In addition, both typical high-angle annular dark-field scanning transmission electron microscope (HAADF-STEM) images and energy-dispersive X-ray (EDX) analysis of KNO/rGO show the presence of C, K, Nb, and O elements (**Figure 1g**), demonstrating the uniform distribution of KNO throughout the whole matrix. The carbon content in KNO/rGO was determined to be 10.1 wt% by thermogravimetric analysis (TGA, **Figures. S4h and S5**) results. Additionally, the HAADF-STEM image of those curly nanosheets indicates that the thickness of the KNO nanosheets is below ten nanometers, in good agreement with the previous observations from SEM images. The N_2 adsorption-desorption spectrum of KNO/rGO (**Figure S6**) indicates an increased

surface area and broader mesoporous distributions. From those microscopic and spectroscopic images, the abundant mesopores around 3.0 nm in size that are well distributed on the KNO surface could provide sufficient interlamination pathways for ion transfer. When combined with the expanded lattice spacing (for the in-plane routes), hierarchical channels will therefore be constructed with an enriched contact area for ions.

The oxidation state and atomic environment have been studied through X-ray photoelectron spectroscopy (XPS), and the results are shown in **Figure 2** and **Figure S7**. Two asymmetric peaks of Nb 3d with the binding energies of 207.1 and 209.8 eV can be observed for the pristine KNO.^[27, 28] In contrast, the lower binding energy values (206.7 and 209.4 eV) (**Figure 2a**) signify that a lower oxidation state existed (eg. Nb⁴⁺) in the KNO/rGO. In addition, two O 1s peaks located at 529.8 and 533.3 eV are found among those proposed samples (**Figure 2b**), which are respectively attributed to the lattice oxygen and near-surface absorbed oxygen.^[9] An intensive peak appearing at 531.7 eV is attributed to oxygen defects for the KNO/rGO sample; the larger peak area further indicates a significant contribution of vacancies compared to the other KNO materials (**Table S1**), which is in agreement with our previous XRD and Raman results. Electron paramagnetic resonance (EPR) measurements also confirm these results, showing a characteristic signal in the fingerprint area that reveals the presence of isolated oxygen vacancies in these samples, while no obvious EPR peak can be detected for the pristine KNO sample (**Figure 2c**). This presence of oxygen vacancies, which leads to change in the electronic structure, can be further confirmed by the color change from white to pale yellow, as shown in **Figure S8**. The introduction of anionic vacancies could induce a certain amount of unsaturated states for the atoms, resulting in the rearrangement of the cationic atoms, and influencing the electrical conduction.^[9] After the vacancies have been introduced into the lattice structure of pristine KNO, the rich population of electrons near the Fermi level (E_F) indicates that better electronic conductivity can be easily achieved (see detailed density

functional theory (DFT) discussions for **Figure S9a and S9b**). At the same time, the bandgap (E_g) of engineered KNO will thus be reduced, as calculated from the UV-visible diffuse-reflectance spectroscopy (**Figure S9c**).

In order to further understand the local electronic environment of Nb, synchrotron based X-ray absorption fine structure (XAFS) measurements were conducted. The related X-ray absorption near-edge spectroscopy (XANES) are shown in **Figure 2d**. In our case, the absorption edge shows a continuous chemical shift to the low-energy side in the order of KNO/rGO > KNO-350 > KNO-200 (inset of **Figure 2d**), indicating a slight reduction of Nb^{5+} to Nb^{4+} when compared to the standard references. Information about the structural parameters and bond distances can be obtained from the extended X-ray absorption fine structure (EXAFS) data, as shown in **Figure 2e and 2f**. As can be seen from the Nb K-edge EXAFS (**Figure 2e**), three peaks that vary in bond length between 0.8 and 2.0 Å represent the niobium–oxygen bonds. Those peaks can be respectively assigned to the short edge-sharing octahedral bonds ($Nb-O_1$), and the long edge-sharing and the uniform corner-sharing bonds ($Nb-O_2$), as well as the additional longer bonds that arise from the layered structure along the b-axis ($Nb-O_3$). The peaks located at around 3.0 Å reflect the Nb–Nb bonds.^[29] The bond lengths and related coordination numbers are acquired by using linear combination fitting, as displayed in **Figure S10 and Table S2**. The low R factors (around 2%) confirm the quality of the fitting. For KNO-350, the corresponding bond lengths of Nb–O are calculated to be 1.88, 2.03 and 2.19 Å, respectively, with the corresponding coordination numbers 1.6, 2.0, and 1.2, providing a total value of 4.8. In contrast, for pristine KNO, the radial distances are changed to 1.87, 2.03, and 2.18 Å, respectively, demonstrating a coordination number of 5.3 in total. The coordination number of Nb–Nb in KNO-350 is increased from 4.8 (pristine KNO) to 7.6, demonstrating the enhanced formation of Nb–Nb bonds in KNO-350. The increased coordination number of Nb–Nb indicates its enhanced metallic nature, which can further improve the conductivity.^[30]

Moreover, the proportion of Nb-O₃ bonds is decreased significantly, resulting in possible dominant sites for vacancy formation (**Table S2**). The reduced bond length for the Nb-Nb bonds and the increased Nb-O bonds demonstrate that slight deformation has occurred due to the higher population of oxygen defects (**Figure 2e**). Those quantitative results further suggest that there are atomic changes during the hydration process. Based on the above characterizations, it is reasonable to conclude that our “blended cocktail strategy” is a successful way to dynamic tailor the atomic structure of the KNO material, which can boost both in-plane and interlamination charge transfer. Those advantages can promote engineered KNO as a promising candidate for high rate electrodes.

To demonstrate the influence of the designed structures on their electrochemical properties, electrochemical testing of the KNO/rGO, KNO-350, KNO-200, and pristine KNO electrodes was systematically conducted (**Figure 3a-3b and Figures. S11-S12**). As can be seen from **Figure 3a**, the charge capacity of KNO/rGO anode after 100 cycles in LIBs is 296.8 mAh g⁻¹, with higher capacity retention when contrasted to the lower 221.7 (pristine KNO), 225.7 (KNO-200), and 253.0 mAh g⁻¹ (KNO-350), respectively. Excellent capacity output of the KNO/rGO electrode was also recorded when cycled at 500 mA g⁻¹ for one thousand cycles (**Figure 3b and Table S3**), which is significantly superior to the performances of KNO-350, KNO-200, rGO, and its commercial H-Nb₂O₅ counter-parts (**Figure S11**). The excellent electrochemical performance of KNO/rGO is not only attributed to the engineered KNO structures but also provided by the rGO. The existence of rGO sheets can provide an effective buffer matrix for the KNO to relieve the volume changes, maintain its structural integrity during electrochemical cycling, and further improve the conductivity.^[10] Compared with the KNO materials without the rGO, the capacity output and rate performance can be further improved. Furthermore, we applied those KNO materials as alternative anodes in PIBs. Currently, only a few works based on niobium and titanium anode materials for PIBs have been reported (**Table S4**).^[31, 32] As can

be seen from **Figure 3c**, KNO/rGO delivers an initial reversible capacity of 414.1 mAh g⁻¹ at 100 mA g⁻¹. After 100 continuous cycles, it maintains capacity of 293.8 mAh g⁻¹ with the average Coulombic efficiency (CE) of 99.72% after initial activation, showing much higher capacity compared to that of the pristine KNO (91.0 mA g⁻¹, K₄Nb₆O₁₇·4.5H₂O). From previous works, it is believed that a certain amount of crystal water may play a positive role in improving the electrochemical activity and enhancing the structural stability due to its ability to screen the electrostatic interactions between exotic alkali ions and the host anions. In our case, however, the preferential solvation of the K⁺ ions with water molecules will result in a destructive structure, which may induce irreversible high local deformations in the crystal structure of the hosts. In addition, the continuous cycling will also result in deintercalation of water from the host, leading to side reactions between the active K metal and water.

To further assess the cycling durability at high current density, KNO based materials were subjected to long-term cycling, as shown in **Figure 3d**. After a continuous 1000 cycles at 500 mA g⁻¹, 231.1 mAh g⁻¹ could be retained, accompanied by approximately 100% coulombic efficiency in KNO/rGO, with the lowest capacity fading-rate (0.004%) when compared to that in KNO-350 (0.012%), KNO-200 (0.035%), and pristine KNO (0.013). In addition, the outstanding capacity retention of KNO/rGO in PIBs is superior to that for LIBs, especially under high current density. Indeed, **Figure 3f** demonstrates that the capacities of KNO/rGO in PIBs at various current densities, ranging from 100 to 5000 mA g⁻¹ are 326.6, 314.7, 290.3, 227.0, 200.0, 175.9, and 149.5 mAh g⁻¹. In particular, nearly 110 mAh g⁻¹ can be achieved when this material subjected to a specific current as large as 10000 mA g⁻¹ (several minutes for completed charge and discharge), which exceeds its rate capability in LIBs (**Figure 3e**). Commercial H-Nb₂O₅, however, exhibits a significantly inferior capacity and cycling performance in PIBs, which is different from the stable capacity output of commercial H-Nb₂O₅ for LIBs (**Figure S11, Figure 3c and 3f**).

1 To gain insight into the relationship between the structures and the electrochemical capability,
 2 cyclic voltammetry curves, electrochemical impedance spectroscopy (EIS), galvanostatic
 3 intermittent titration technique (GITT) tests, ex-situ XRD, and DFT calculations were
 4 conducted, as shown from **Figures. S13 to S16**. As revealed in Figure S13a, the slope of the
 5 peak intensity (denoted as the b-value) of the cathodic peak in KNO/rGO for LIBs was
 6 calculated to be around 0.92, making it manifest that the current originates from a
 7 pseudocapacitive dominated mechanism.²⁰ The quantitatively separated contributions of the
 8 capacitive part increased from 64.0 % at 0.5 mV s⁻¹ (**Figure S13b**) to the maximum value of
 9 85 % at 5.0 mV s⁻¹ in LIBs, which is much higher than that in pristine KNO (39% and 63%,
 10 respectively), demonstrating the increased pseudocapacitive contribution in KNO/rGO. The
 11 corresponding b-value of KNO/rGO for PIBs is quite similar to that for LIBs (**Figure S13c**),
 12 indicating a maximum contribution of 84 % of the capacitive part at 5.0 mV s⁻¹. Moreover, a
 13 much lower ohmic resistance value can be found in KNO/rGO in both LIBs and PIBs (**Figure**
 14 **S14**), suggesting faster electron charge transfer kinetics, as we discussed in connection with
 15 the DOS calculations and diffuse reflectance spectrum (**Figure S9**). In addition, the quasi-
 16 thermodynamic equilibrium potential and K ion diffusivity coefficients for KNO materials
 17 were systematically measured by using the GITT after five charge/discharge activation cycles.
 18 As can be seen from Figure S15, the calculated potassium diffusion coefficients, on the order
 19 of 10⁻⁸–10⁻¹⁰ cm² s⁻¹ in both charge and discharge of KNO-350, are markedly faster than that
 20 of the pristine KNO. More interesting, the diffusion coefficients are one order of magnitude
 21 higher than those of Li⁺ in both the intercalation/deintercalation processes (**Figure S15e** and
 22 **S15f**), which results in the better transfer kinetics of KNO-350 in PIBs. This indicates the
 23 formation of a favourable structure for K ion insertion/de-insertion in engineered KNO
 24 materials, which can be achieved by our “blended cocktail strategy”.

1 DFT simulations were conducted to further understand the possible migration pathways and
 2 correlated energy barriers for both Li^+ and K^+ along different paths in both pristine KNO and
 3 engineered KNO materials (**Figure 4**). For pristine KNO, four typical diffusion paths were
 4 considered, and the related migration paths and corresponding barriers are shown in **Figure 4a**
 5 **and 4c**. The barrier to transfer from A to D sites is calculated to be 0.27 eV, whereas the barriers
 6 from A to B, C, and E sites are 0.62, 0.43, and 0.29 eV, respectively, indicating that the K ions
 7 migration in pristine KNO is mainly through the interlayer channels along the reverse direction
 8 of the b-axis. In comparison to the pristine KNO, aided by the expansion of the lattice spacing
 9 with vacancies, the engineered KNO (red lines in **Figure 4c**) shows much lower migration
 10 barriers of 0.20 (A to D), 0.28 (A to B), and 0.43 eV (A to C) along these paths. Interestingly,
 11 the most optimized migration path for K ions is along the b-axis direction with a barrier of only
 12 0.15 eV (A to E), which is significantly lower than that in pristine KNO. The much lower
 13 energy barriers in engineered KNO further indicate that the K ions could be transferred along
 14 several directions by forming interlinked migration paths, which is superior to the
 15 unidirectional migration in pristine KNO. Moreover, to compare the intercalation kinetics of
 16 Li and K ions within the engineered KNO, the Li diffusion barrier was also calculated, as shown
 17 by the yellow lines in **Figure 4b and 4d**. Obviously, the corresponding energy barriers of the
 18 A-B, A-C, A-D, and A-E paths in LIBs are 0.73, 1.42, 1.10, and 1.08 eV, respectively, much
 19 higher compared to those in PIBs. The lowest energy barrier for Li diffusion in engineered
 20 KNO, is still much higher than that for K ion migration, demonstrating its favourable K ion
 21 transfer kinetics.^[33, 34] Unlike previous reports that K ions suffer from sluggish diffusion in
 22 solid-state electrode materials, our observations indicate that the engineered KNO exhibits
 23 higher K^+ diffusion kinetics compared to Li^+ . We attribute the excellent potassium storage to two
 24 dominant factors. Firstly, the energy barrier for Li diffusion in engineered KNO is much higher than
 25 that for K ion migration, demonstrating the favorable K ion transfer kinetics in engineered KNO.

Secondly, the usual applied electrolyte (1.5 M KFSI in EC/DEC) in potassium ion batteries may produce a stable SEI layer compared to that with lithium storage (1 M LiPF₆ in EC/DEC).^[31]

The KNO/rGO, due to its structural benefits, kinetics advantages, and physical merits, has already been demonstrated as a promising anode in a half-cell system, but its practical application as an anode in PIBs was further evaluated in a full-cell with a perylene-3, 4, 9, 10-tetracarboxylic dianhydride (PTCDA) cathode. PTCDA was chosen as a suitable cathode owing to its highly stable capacity output, cost-effectiveness, and interesting voltage platform in the selected electrolyte range from 1.5V to 3.5V (**Figure S17**).^[35] As discussed in previous works, the electrolyte plays a crucial role in the cathode-electrolyte interphase (CEI) layer formation and could significantly influence the PIB performance. Therefore, 1.5 M KFSI in EC/DEC was chosen due to its excellent solubility and ionic mobility in both KNO anode and PTCDA cathode (**Figure 5a and 5b**) compared to other kinds of electrolyte. Two platforms located at 2.1 and 1.5 V can be found in the discharge curves (**Figure S18**) and the full battery exhibits remarkable cycling stability (**Figure 5c**) with a stable capacity of 192.7 mAh g⁻¹ over 300 continuous cycles, which is highly competitive with currently reported full PIB cells. On the basis of the electrochemical and theoretical analysis, the strategy of using a dehydration process for the construction of ionic channels could be an effective way to improve the high rate performance. The as-designed hierarchical ionic channels could dramatically improve the charge transfer with reduced energy barriers, which dramatically enhanced the electrochemical performance not only of LIBs but also of PIB.

3. Conclusion

In conclusion, engineered KNO nanosheets with designed ionic channels have been successfully fabricated by a facile method. The combined experimental and theoretical calculations demonstrate that the construction of hierarchical ionic channels on the atomic level can effectively improve the structural flexibility and diffusion barriers, resulting in improved electronic and ionic kinetics. As a result, the ultra-long cycling stability of KNO under high current densities in both lithium and potassium ion batteries have been demonstrated. In this regard, our design strategy paves a new way to achieve the fabrication of promising electrode materials, by tuning the microstructures on the atomic-scale for ready uptake of alkali ions or other ions with a larger radius, so this “blended cocktail strategy” could be extended to other energy storage and conversion materials in the future.

4. Experimental Section

Synthesis of potassium niobium oxide:

The potassium niobium oxide was prepared by a homogeneous precipitation method. In a typical synthesis process, a mixture of niobium oxide powder (Sigma-Aldrich) dissolved in 3 M potassium hydroxide solution was first magnetically stirred for 120 minutes. Then, the above solution was transferred to a sealed autoclave, which was kept in an oven at 180 °C for 10 h until a clear solution was obtained. After the autoclave was cooled down to room temperature, several grams of urea were slowly added into the solution with vigorous stirring for another 120 minutes, after which, the concentration of the potassium hydroxide solution was adjusted to 0.5 M with deionized water. Subsequently, the solution was transferred to a sealed autoclave and kept in an oven at 200 °C overnight. The product was finally obtained by centrifugation, along with washing several times in de-ionized water and ethanol. The resultant material was dried at 70 °C for 12 h, yielding the pristine potassium niobium oxide (KNO) nanosheets.

Around 2.0 g obtained KNO was then treated at different temperatures ranging from 200 to 500 °C, respectively, with a ramping rate of 10 °C min⁻¹ and kept at each target temperature for 3 h under H₂ (5 vol%) /Ar (95 vol%) to acquire the KNO-200, KNO-300, KNO-350, and KNO-500 samples.

Synthesis of graphene oxide coated potassium niobium oxide:

Graphite oxide, initially prepared by a modified Hummers' method was dispersed into 20 mL of water.^[10] Then, 300 mg of pristine KNO was added with a certain amount of cetyltrimethylammonium bromide (CTAB) into the above solution. After continuous stirring for 12 h at 60 °C, the resulting homogeneous aqueous dispersion was lyophilized, followed by a reduction in a tube furnace at 350 °C for the duration of 3 h under H₂ (5 vol%)/Ar (95 vol%) atmosphere to achieve the KNO/rGO composites.

Materials characterization:

The morphologies of the as-prepared products were observed by field emission scanning electron microscopy (FESEM, JEOL JSM-7500FA) operated at 15 kV and 20 mA. The details of the crystal structure were further examined by scanning transmission electron microscope (STEM, JEOL JEM-ARM200F), which was conducted at 200 kV, along with energy dispersive X-ray spectroscopy (EDX) mapping. The crystalline structure of the obtained materials was determined by X-ray diffraction (XRD, PANalytical instrument) with Cu K α radiation at a scanning rate of 10° min⁻¹.

X-ray photoelectron spectroscopy (XPS) was conducted on a VG Multilab 2000 (VG Inc.) photoelectron spectrometer using monochromatic Al K α radiation under vacuum at 2×10^{-6} Pa. The data acquisition and analysis were conducted with CasaXPS (Casa Software Ltd.). All of the binding energies were referenced to the C 1s peak position at 284.8 eV of the surface adventitious carbon. Synchrotron X-ray absorption spectroscopy (XAS) measurements were conducted at the wiggler XAS Beamline (12ID) at the Australian Synchrotron in Melbourne, by using a set of liquid nitrogen cooled Si (311) monochromator crystals. The measurements were performed at the Nb K-edge (18.99 keV) in beamline Mode 3 in Hutch B. The data reduction followed standard methods using the ATHENA software package. Calibrations and structural refinements were carried out using Nb metal as a reference. First-shell data analyses were performed under the assumption of single scattering, with error estimations given by the R-factor.

Fourier transform infrared (FT-IR) spectra were obtained on a Shimadzu FTIR Prestige-21. Inductively coupled plasma atomic emission spectroscopy (ICP-AES; Thermo Scientific) analysis was used to determine the contents of potassium, niobium, and carbon in the KNO₃ based materials. Raman analysis was performed with a JobinYvon HR800 Raman spectrometer. Continuous-wave electron paramagnetic resonance (EPR) experiments were conducted on a Bruker ELEXSYS E580 spectrometer operating in the X-band (9.4 GHz) mode

and equipped with an Oxford CF935 helium flow cryostat with an ITC-5025 temperature controller. Thermogravimetric analysis (TGA) was conducted on a Mettler Toledo TGA/DSC1 analyzer from 50 to 1000 °C in air (20 sccm) with a ramp rate of 5 °C min⁻¹. Ultraviolet-visible (UV-vis diffuse) reflectance spectra were collected on a Shimadzu UV-3600 Plus UV-VIS-NIR Spectrophotometer with an integrating sphere.

To break up KNO/rGO and KNO materials to thin nanosheets, the samples were first dispersed in ethanol and sonicated for 1 h using a horn-probe tip Sonicator (Sonics Vibra-cell VCX-750W) operating at 25% amplitude and 3 s on and 3 s off pulses while the dispersion was cooled in an ice bath. The resultant dispersion was then centrifuged for 30 min at 1500 rpm to remove the unexfoliated residue. Those thin nanosheets were then collected by centrifugation for 15 min at the speed of 12000 rpm, washed, and lyophilized. Atomic force microscopy (AFM) was conducted on an Asylum AFM (Oxford Instruments, United Kingdom).

Electrochemical Tests:

The electrochemical tests were conducted using CR 2032 coin-type cells. All working electrodes were prepared by mixing the obtained materials, Super P, carboxymethyl cellulose (CMC), and poly (acrylic acid) (PAA) in a weight ratio of 80:10:5:5. The resultant slurry was pasted on Cu foil and dried at 150 °C for 3 h in a vacuum oven, followed by pressing at 20 kg cm⁻². Commercially available H-Nb₂O₅ purchased from Sigma-Aldrich and homemade rGO were used in this work without further purification. The mass loading of the materials on individual electrodes was about 1.0–1.5 mg cm⁻². Electrochemical measurements were carried out using two-electrode coin cells with Li or K metal as counter or reference electrodes, and Celgard (product 2400) film and Whatman glass fiber film (GF/D) as the separator for lithium and potassium ion batteries, respectively. The electrolyte for lithium storage consisted of a solution of 1 M lithium hexafluorophosphate (LiPF₆) in ethylene carbonate (EC)/diethyl carbonate (DEC) (1:1; v/v), and for potassium storage the electrolytes used consisted of

1 solutions of 1.5 M potassium bis(fluoro sulfonyl)imide (KFSI) in EC/DEC (1:1; v/v), 0.8 M
2 potassium hexafluorophosphate (KPF₆) in EC/DEC(1:1; v/v), 1 M KFSI in propylene
3 carbonate (PC), and 1 M KFSI in dimethyl ether (DME), respectively. Electrochemical
4 impedance spectroscopy and cyclic voltammetry were conducted on a VMP-3 electrochemical
5 workstation with a scan rate range from 0.1 mV s⁻¹ to 20 mV s⁻¹. Galvanostatic intermittent
6 titration technique (GITT) tests were also conducted on an Arbin SCTS battery tester at ambient
7 temperature in the voltage range of 0.01–2.0 V. To activate the electrodes, the cells were
8 galvanostatically charged/discharged in the voltage range of 0.01–2.0 V versus Li/Li⁺ and K/K⁺
9 at different current densities on a Neware battery tester. Nyquist plots were obtained over the
10 frequency range of 100 kHz to 1 Hz. For the ex-situ measurements, the tested electrochemical
11 cells in different states of charge/discharge were disassembled in an Ar-filled glove box. The
12 electrodes were taken out and rinsed in anhydrous diethyl carbonate to remove residual salts.

13 The full-cell was assembled by using perylene-3, 4, 9, 10-tetracarboxylic dianhydride
14 (PTCDA) as the cathode and KNO/rGO as the anode. The PTCDA was first annealed at 450
15 °C for 5 h under Ar with a heating rate of 10 °C min⁻¹, as previously reported, and then the
16 treated PTCDA was mixed with Super P, CMC, and PAA in a weight ratio of 80:10:5:5. A
17 homogeneous slurry was first obtained by using a mixed solution of water and ethanol (4:1,
18 v/v), then pasted onto carbon-coated aluminum foil, and further placed in a vacuum oven for 3
19 h at 150 °C. The average areal mass loading on an individual treated PTCDA cathode was
20 about 2.0-2.5 mg cm⁻². The prepotassiated KNO/rGO anode, with a loading of around 0.8 mg
21 cm⁻², was obtained by cycling for 10 cycles. The treated PTCDA cathode was also cycled 10
22 times before being assembled in the full cell for testing in the voltage range of 0.8 to 2.8 V.
23 The separators were glass fiber (Whatman GF/A), and the dosage of 1.5 M KFSI EC/DEC
24 electrolyte for each coin cell was 50 µL. All capacities were calculated based on the anode
25 material.

The degree of pseudocapacitive effect can be qualitatively calculated by the relationship between the measured peak current (i) for an individual peak and the scan rate (v) acquired from the cyclic voltammetry (CV) curves:

$$i = kv^b \quad (1)$$

where k and b both are constants. The value of b is between 0.5 and 1.0, which is determined from the slope of the $\log i$ versus $\log v$ plot. It is well known that for a diffusion-dominated reaction, b always reaches 0.5, while b is close to 1.0 for a surface capacitance-controlled process. The contributions to the capacity can be further quantified by the following equation:

$$i = k_1v + k_2 v^{1/2} \quad (2)$$

where k_1v and $k_2v^{1/2}$ represent the pseudocapacitive and diffusion-dominant contributions, respectively.

For the GITT tests, the anodes were tested after five charge/discharge activation cycles. The ionic diffusion coefficient (D_{Li^+} or D_{K^+}) in the KNO electrodes could be determined by solving Fick's second law using the following equations based on the GITT curves, where m_a is the electrode active mass; M_a is the molar mass of the electrode material; V_M is the molar volume of the electrode; S is the geometric area of the electrode; M_a/V_M is obtained from the density of the electrode; and L is the average thickness of the electrode. τ is the period of the pulse.

$$D = \frac{4}{\pi\tau} \left(\frac{m_a V_M}{M_a S} \right)^2 \left(\frac{\Delta E_s}{\tau \times \frac{dE_s}{d\sqrt{\tau}}} \right)^2 \quad (\tau \ll L^2/D) \quad (3)$$

If the coin cell voltage is linearly proportional to $\tau^{1/2}$, Equation (3) can be further simplified to the following Equation (4):

$$D = \frac{4}{\pi\tau} \left(\frac{m_B V_M}{M_B S} \right)^2 \left(\frac{\Delta E_s}{\Delta E_\tau} \right)^2 \quad (4)$$

Density Functional Theory Calculations

The theoretical calculation were performed via density functional theory plus Hubbard correction (DFT + U) calculations enabled by VASP code, and the generalized gradient

approximation (GGA) with the Perdew-Burke Ernzerhof (PBE) functional was employed for the exchange-correlation function. In this part, the projector augmented plane-wave (PAW) method was used to describe electrons. The kinetic energy cut-off was set at 600 eV. During the optimization, the force and energy respectively converged to 0.01 eV/Å and 10^{-6} eV /atom, with both the atoms' positions and the lattice parameters allowed to relax.

To probe the validity of our computational approach, structural optimizations of $\text{K}_4\text{Nb}_6\text{O}_{17}$ were first presented based on the bulk crystal structure that was observed experimentally. That is, the crystal structure of pristine $\text{K}_4\text{Nb}_6\text{O}_{17}$ is orthorhombic (space group P21nb), composed of edge- and corner-sharing NbO_6 octahedra. The energy barriers for Li or K ion diffusion in KNO materials were computed with the climbing nudged elastic band (CINEB) method. For pristine KNO, four typical diffusion paths were considered. Among them, the “A” site is in the middle of the supercell, while the B and C sites are along the two directions of the c-axis close to the ab-plane, and the D and E sites are along the two directions of the b-axis close to the ac-plane.

Supporting Information

Supporting Information is available from the Wiley Online Library or from the author.

Acknowledgements

Financial supports provided by the Australian Research Council (ARC) (FT150100109, DP170102406, DP200101862, and DE190100504) is gratefully acknowledged. All the authors discussed the results and commented on the manuscript. The authors thank the Electron Microscopy Centre (EMC) at the University of Wollongong. The authors also thank Prof. Yang Zheng, Dr. Guoqiang Zhao, Fuhua Yang, and Nana Liu for their help with AFM and full cell tests and Dr. T. Silver for critical reading of the

1 manuscript. The authors would also like to thank AINSE Ltd for providing financial assistance (Award
2 – PGRA).

3
4
5
6
7

Received: ((will be filled in by the editorial staff))
Revised: ((will be filled in by the editorial staff))
Published online: ((will be filled in by the editorial staff))

References

- [1] C. Tan, X. Cao, X.-J. Wu, Q. He, J. Yang, X. Zhang, J. Chen, W. Zhao, S. Han, G.-H. Nam, *Chem. Rev.*, **2017**, *117*, 6225-6331.
- [2] Y. Liu, C. Xiao, P. Huang, M. Cheng, Y. Xie, *Chem*, **2018**, *4*, 1263-1283.
- [3] Y. Lu, L. Yu, M. Wu, Y. Wang, X. W. Lou, *Adv. Mater.*, **2018**, *30*, 1702875.
- [4] S. Zhang, Y. Zheng, X. Huang, J. Hong, B. Cao, J. Hao, Q. Fan, T. Zhou, Z. Guo, *Adv. Energy Mater.*, **2019**, *9*, 1900081.
- [5] Y. Xu, M. Zhou, X. Wang, C. Wang, L. Liang, F. Grote, M. Wu, Y. Mi, Y. Lei, *Angew. Chem. Int. Ed.*, **2015**, *54*, 8768-8771.
- [6] T. Koketsu, J. Ma, B. J. Morgan, M. Body, C. Legein, W. Dachraoui, M. Giannini, A. Demortière, M. Salanne, F. Dardoize, *Nat. Mater.*, **2017**, *16*, 1142-1148.
- [7] Y. Zeng, Z. Lai, Y. Han, H. Zhang, S. Xie, X. Lu, *Adv. Mater.*, **2018**, *30*, 1802396.
- [8] H. Sun, J. Zhu, D. Baumann, L. Peng, Y. Xu, I. Shakir, Y. Huang, X. Duan, *Nat. Rev. Mater.*, **2019**, *4*, 45-60.
- [9] Y. Zheng, T. Zhou, X. Zhao, W. K. Pang, H. Gao, S. Li, Z. Zhou, H. Liu, Z. Guo, *Adv. Mater.*, **2017**, *29*, 1700396.
- [10] Y. Zheng, T. Zhou, C. Zhang, J. Mao, H. Liu, Z. Guo, *Angew. Chem. Int. Ed.*, **2016**, *55*, 3408-3413.
- [11] J. Hao, J. Long, B. Li, X. Li, S. Zhang, F. Yang, X. Zeng, Z. Yang, W. K. Pang, Z. Guo, *Adv. Funct. Mater.*, **2019**, *29*, 1903605.
- [12] A. C. Forse, J. M. Griffin, C. Merlet, J. Carretero-Gonzalez, A.-R. O. Raji, N. M. Trease, C. P. Grey, *Nat. Energy*, **2017**, *2*, 1-7.
- [13] Y. Li, Y. Lu, P. Adelhelm, M.-M. Titirici, Y.-S. Hu, *Chem. Soc. Rev.*, **2019**, *48*, 4655-4687.
- [14] S. Zhang, F. Yao, L. Yang, F. Zhang, S. Xu, *Carbon*, **2015**, *93*, 143-150.
- [15] Y. Wen, K. He, Y. Zhu, F. Han, Y. Xu, I. Matsuda, Y. Ishii, J. Cumings, C. Wang, *Nat.*

- 1 *Commun.*, **2014**, *5*, 1-10.
- 2 [16] W. Yang, J. Zhou, S. Wang, W. Zhang, Z. Wang, F. Lv, K. Wang, Q. Sun, S. Guo, *Energy*
- 3 *Environment. Sci.*, **2019**, *12*, 1605-1612.
- 4 [17] D.-S. Bin, X.-J. Lin, Y.-G. Sun, Y.-S. Xu, K. Zhang, A.-M. Cao, L.-J. Wan, *J. Ame. Chem.*
- 5 *Soc.*, **2018**, *140*, 7127-7134.
- 6 [18] J. Bai, B. Xi, H. Mao, Y. Lin, X. Ma, J. Feng, S. Xiong, *Adv. Mater.*, **2018**, *30*, 1802310.
- 7 [19] J. Zhou, L. Wang, M. Yang, J. Wu, F. Chen, W. Huang, N. Han, H. Ye, F. Zhao, Y. Li, *Adv.*
- 8 *Mater.*, **2017**, *29*, 1702061.
- 9 [20] Q. Deng, Y. Fu, C. Zhu, Y. Yu, *Small*, **2019**, *15*, 1804884.
- 10 [21] V. Augustyn, J. Come, M. A. Lowe, J. W. Kim, P.-L. Taberna, S. H. Tolbert, H. D. Abruña, P.
- 11 Simon, B. Dunn, *Nat. Mater.*, **2013**, *12*, 518-522.
- 12 [22] K. J. Griffith, K. M. Wiaderek, G. Cibir, L. E. Marbella, C. P. Grey, *Nature*, **2018**, *559*, 556-
- 13 563.
- 14 [23] Y. Kobayashi, H. Hata, M. Salama, T. E. Mallouk, *Nano. Lett.*, **2007**, *7*, 2142-2145.
- 15 [24] K. Nassau, J. Shiever, J. Bernstein, *J. Electrochem. Soc.*, **1969**, *116*, 348-353.
- 16 [25] H. T. Kreissl, M. M. Li, Y.-K. Peng, K. Nakagawa, T. J. Hooper, J. V. Hanna, A. Shepherd,
- 17 T.-S. Wu, Y.-L. Soo, S. E. Tsang, *J. Ame. Chem. Soc.*, **2017**, *139*, 12670-12680.
- 18 [26] J. M. Jehng, I. E. Wachs, *Chem. Mater.*, **1991**, *3*, 100-107.
- 19 [27] F. Liu, X. Cheng, R. Xu, Y. Wu, Y. Jiang, Y. Yu, *Adv. Funct. Mater.*, **2018**, *28*, 1800394.
- 20 [28] H. Park, H. B. Wu, T. Song, X. W. Lou, U. Paik, *Adv. Energy Mater.*, **2015**, *5*, 1401945.
- 21 [29] M. A. Bizeto, F. Leroux, A. L. Shiguihara, M. L. A. Temperini, O. Sala, V. R. L. Constantino,
- 22 *J. Phys. Chem. Solids*, **2010**, *71*, 560-564.
- 23 [30] H. Wang, J. Zhang, X. Hang, X. Zhang, J. Xie, B. Pan, Y. Xie, *Angew. Chem. Int. Ed.*, **2015**,
- 24 *54*, 1195-1199.
- 25 [31] Q. Zhang, Z. Wang, S. Zhang, T. Zhou, J. Mao, Z. Guo, *Electrochem. Energy Rev.*, **2018**, *1*,

625-658.

[32] H. Che, S. Chen, Y. Xie, H. Wang, K. Amine, X.-Z. Liao, Z.-F. Ma, *Energy Environment. Sci.*, **2017**, *10*, 1075-1101.

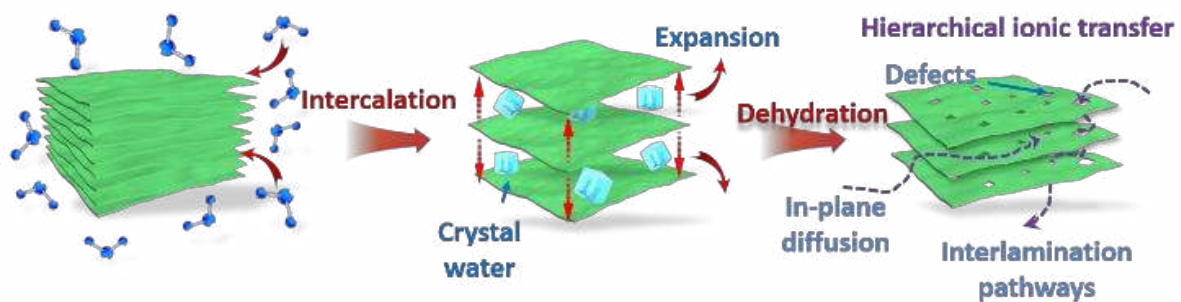
[33] L. Yang, X. Zhu, X. Li, X. Zhao, K. Pei, W. You, X. Li, Y. Chen, C. Lin, R. Che, *Adv. Energy Mater.* **2019**, *9*, 1902174.

[34] G. Zhu, Q. Li, Y. Zhao, R. Che, *ACS Appl. Mater. Interfaces*, **2017**, *9*, 41258-41264.

[35] L. Fan, R. Ma, J. Wang, H. Yang, B. Lu, *Adv. Mater.*, **2018**, *30*, 1805486.

1

2



3 **Scheme 1.** Synthetic route for the engineered KNO via the dehydration process.

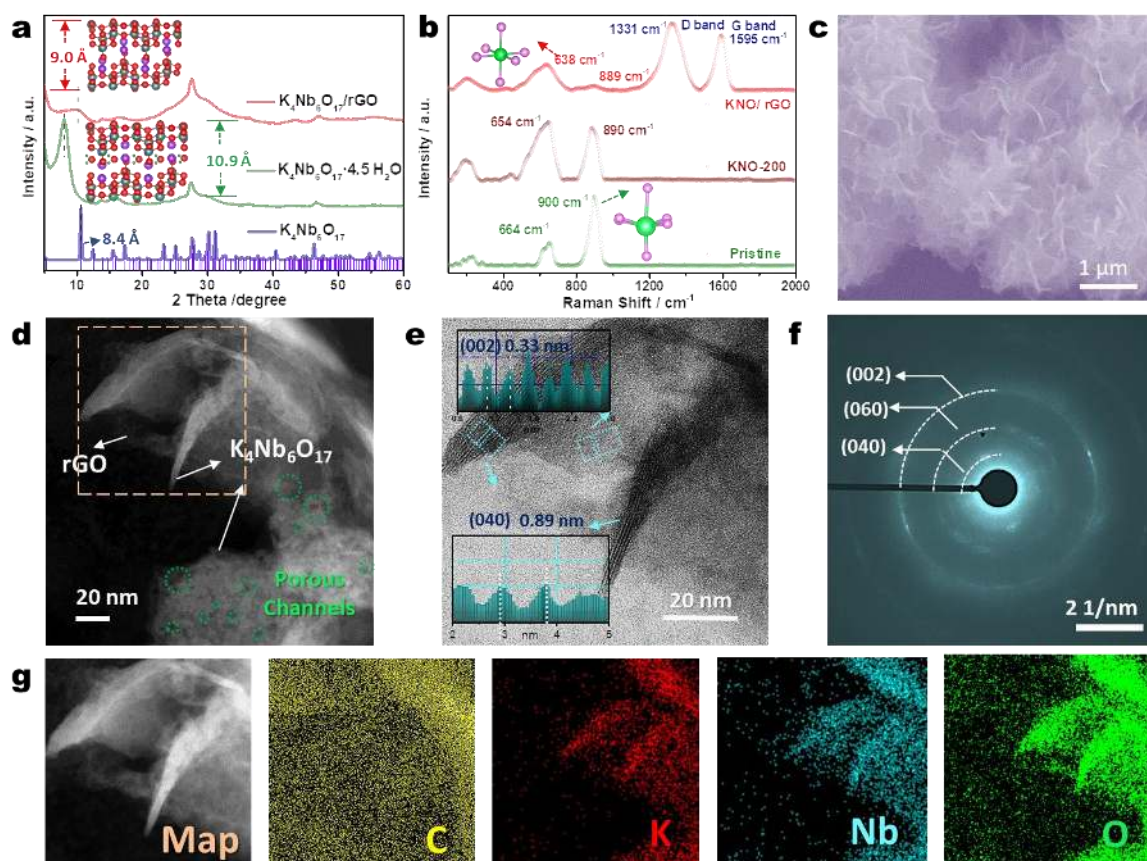


Figure 1. Characterization of the KNO-based materials. a) XRD patterns; Insets: crystal structures of the KNO and KNO/rGO viewed along the [040] direction. Green balls indicate the Nb atoms, purple represents the K atoms, grey-green dots indicate the H atoms, and the red atoms belong to O element. The pink dots are from the standard XRD pattern of $\text{K}_4\text{Nb}_6\text{O}_{17}$. b) Raman spectra, with the NbO_6 octahedra shown in the insets. The Raman peaks located at 1331 and 1595 cm^{-1} can be indexed to rGO. c) Typical SEM image of pristine KNO. d) HAADF-STEM image and e) its corresponding TEM image of typical KNO/rGO nanosheets. The green circles in d) indicate porous structures. The clear crystalline planes with a d -spacing of 0.33 nm in e) can be ascribed to the (002) planes of KNO (top inset) and those with 8.9 \AA to the (040) planes (bottom inset). f) Typical SAED pattern derived from KNO/rGO. g) The corresponding elemental mapping images of the selected area outlined in yellow of image d).

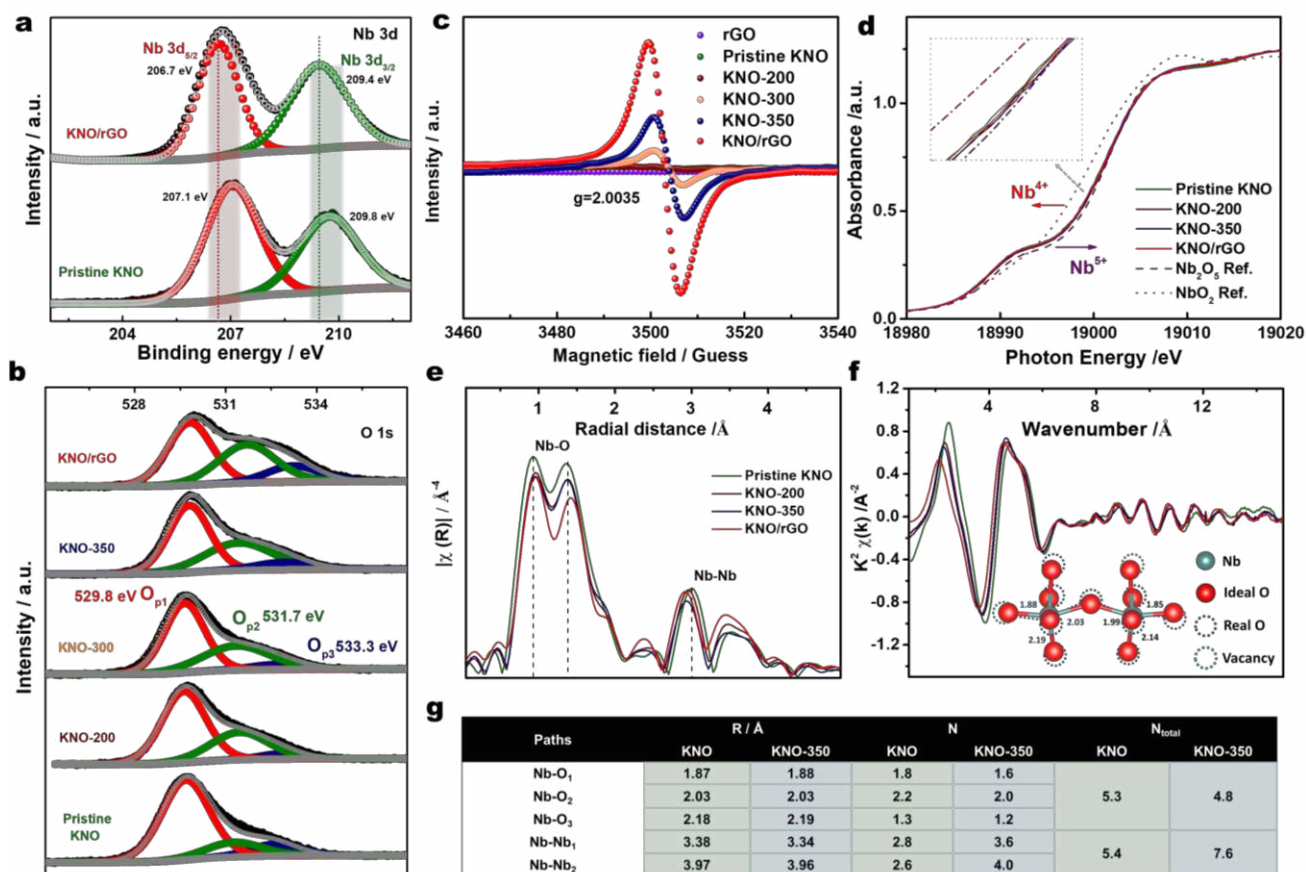


Figure 2. Understanding of the fine structure of the KNO-based materials. a) The corresponding XPS spectra of Nb 3d for pristine KNO and KNO/rGO. b) XPS spectra of O 1s for the samples. The new peak located at 531.7 eV reflects the generated oxygen vacancies. c) EPR spectra, where there is a gradually changing signal from KNO-300 to KNO/rGO, indicating the variable content of oxygen vacancies in the KNO sheets. d) Normalized XANES Nb K-edge absorption spectra with enlargement in the inset. e) EXAFS spectra of Nb K-edge plotted in R space. f) EXAFS spectra of Nb K-edge plotted in K space. The shift of Nb-O bonds towards higher bond length, as shown in the inset, indicates that that defect content gradually varied from pristine KNO to KNO/rGO. g) Fitted results for pristine KNO and KNO-350 derived from the EXAFS data.

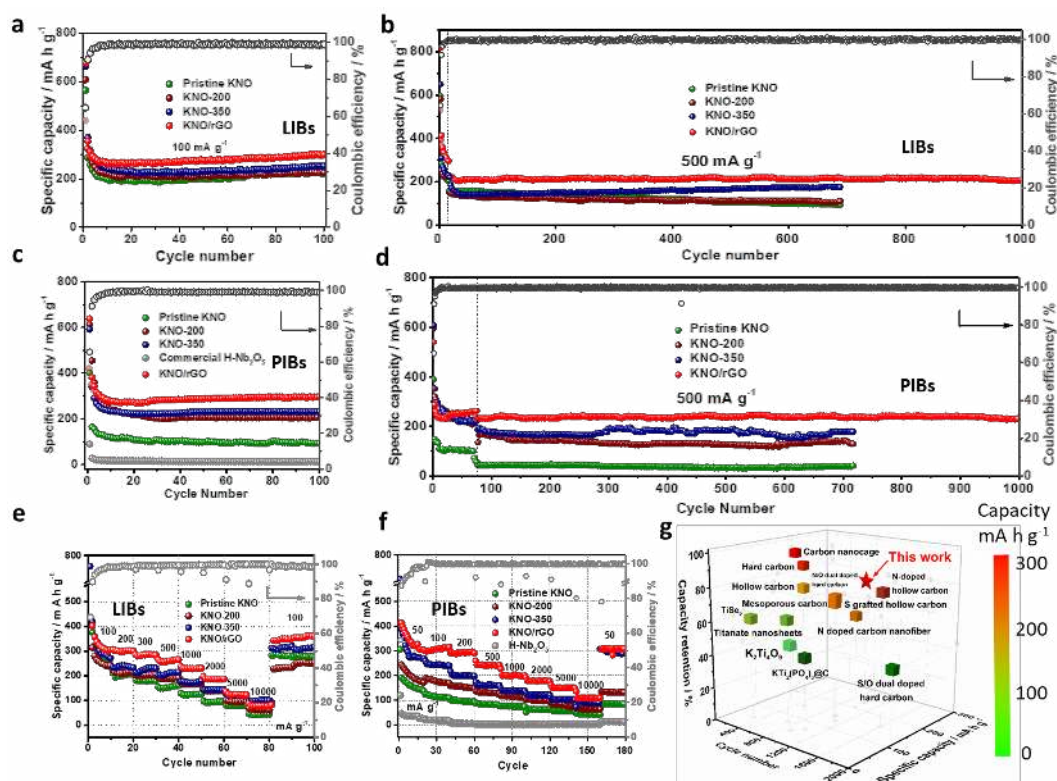


Figure 3. Electrochemical characterizations of KNO-based anodes for Lithium/Potassium ion batteries. a) Cycling performance of LIBs acquired under a current density of 100 mA g⁻¹. b) Long-term cycling stability for LIBs at a current density of 500 mA g⁻¹. c) Cycling performance for potassium ion batteries (PIBs) acquired under a current density of 100 mA g⁻¹. d) Long cycling stability for PIBs under a current density of 500 mA g⁻¹. Rate capabilities for e) LIBs and f) PIBs. g) Comparison of recently reported niobium, titanium, and carbon-based materials in potassium-ion batteries; the specific capacities are based on Table S4. All the coulombic efficiencies are plotted here for KNO/rGO only.

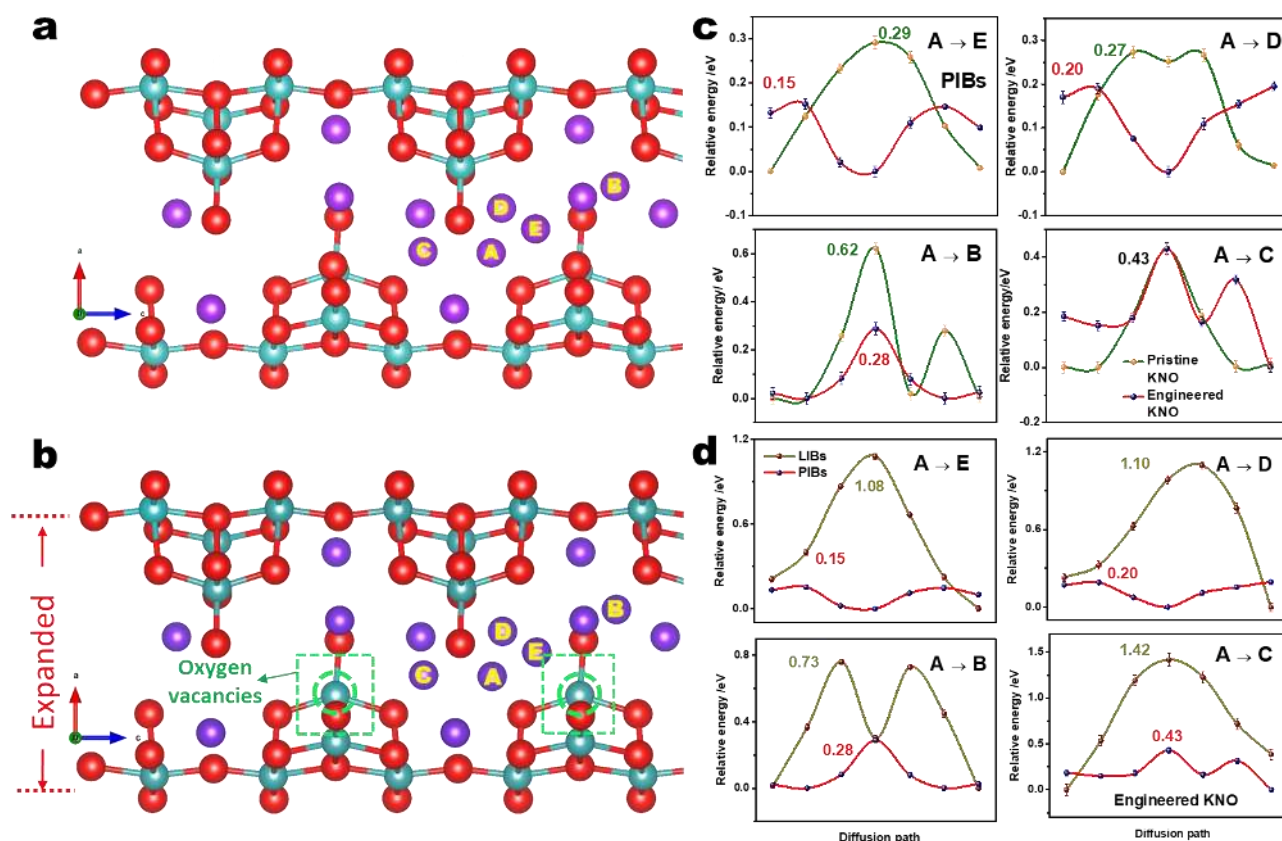


Figure 4. Crystal structure, diffusion paths, and corresponding migration energy barriers calculated by DFT simulations. a) Crystal structure of pristine KNO with representative K ions intercalated at A, B, C, D, and E sites. b) Crystal structure of engineered KNO and typical intercalation sites. Purple represents K, blue represents Nb, and red stands for oxygen atoms. The green circles indicate the vacancy sites. c) Comparison of calculated migration energy barriers opposing K⁺ diffusion through multiple paths in both pristine KNO (green) and engineered KNO (red). d) Comparison of calculated migration energy barriers opposing Li⁺ (yellow) and K⁺ (red) diffusion along various paths in engineered KNO. The error bars represent the standard deviation of the values.

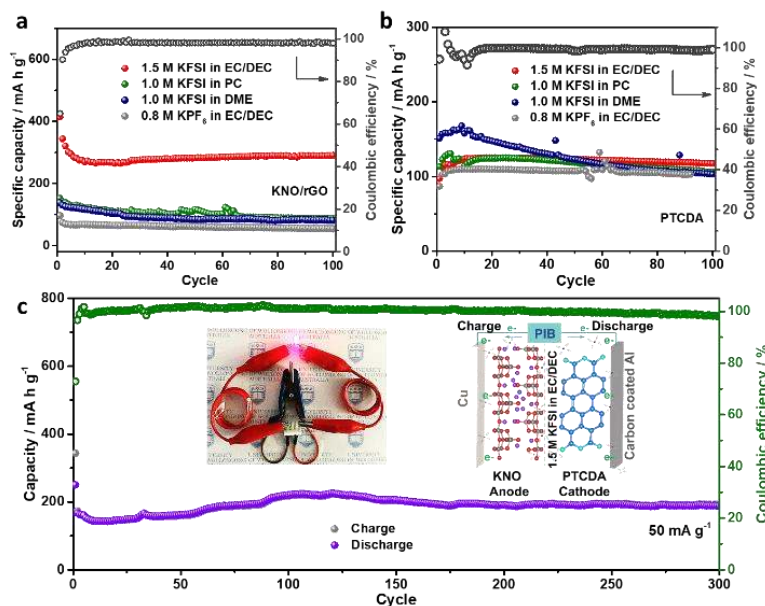


Figure 5. Full-cell performance of KNO/rGO. Potassium-ion full-cell electrochemical performance of KNO/rGO: a) Cycling performance of KNO/rGO in different electrolytes acquired under a current density of 100 mA g⁻¹. b) Cycling performance of PTCDA in different electrolytes, acquired under a current density of 100 mA g⁻¹. c) Long-term cycling performance at 50 mA g⁻¹ for the full cell, schematic illustration of PTCDA||KNO/rGO full-cell configuration (right inset), and photograph of full-cell (left in-set). This outstanding performance of the full cell indicates that PTCDA|| KNO/rGO can serve as a promising cell for practical application.

Keyword: ionic channel engineering, dehydration process, energy storage, atomic structural engineering, density functional calculations

Shilin Zhang, Qining Fan, Ye Liu, Shibo Xi, Xiufan Liu, Zhibin Wu, Junnan Hao, Wei Kong Pang, Tengfei Zhou*, Zaiping Guo*

Dehydration-triggered Ionic Channel Engineering in Potassium Niobate for Li / K ion Storage

ToC

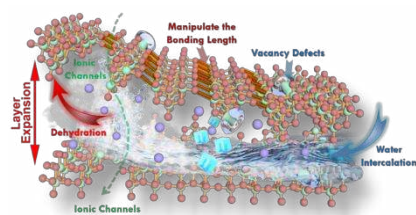


Table of Contents: The schematic illustration of ionic rearrangements and distortions derived from dehydration engineering.